

Nonlocal signatures of hybridization between quantum dot and Andreev bound states

Andreas Pöschl,¹ Alisa Danilenko,¹ Deividas Sabonis,^{1,2} Kaur Kristjuhan,¹ Tyler Lindemann,³ Candice Thomas,³ Michael J. Manfra,^{3,4} and Charles M. Marcus¹

¹*Center for Quantum Devices, Niels Bohr Institute, University of Copenhagen, 2100 Copenhagen, Denmark*

²*Laboratory for Solid State Physics, ETH Zürich, CH-8093 Zürich, Switzerland*

³*Department of Physics and Astronomy, and Birck Nanotechnology Center, Purdue University, West Lafayette, Indiana 47907 USA*

⁴*School of Materials Engineering, and School of Electrical and Computer Engineering, Purdue University, West Lafayette, Indiana 47907 USA*

We investigate local and nonlocal signatures of hybridization between a quantum dot state and an extended Andreev bound state (ABS) in a gate-defined InAs nanowire with multiple side probes. When a quantum dot in one of the side probes was hybridized with an ABS in the nanowire, a characteristic spectroscopic pattern was observed both locally, i.e., in the probe with the quantum dot, and nonlocally, in the tunnel conductance of a remote probe. Nonlocal signatures of hybridization reveal the extended nature of the ABS.

Progress in material growth has enabled the realization of hybrid materials with distinct low-temperature phases [1–4] not observed in the constituent bulk materials [5–11]. An important example is a superconductor grown epitaxially on a semiconductor having gateable carrier density, large negative g -factor, and strong spin-orbit coupling [12–14]. A promising material platform that allows for scalable fabrication of advanced devices in this context are InAs two-dimensional electron gases (2DEGs) proximitized by superconducting Al [15–21]. Devices of suitable geometries allow exploration of various bound states in nanowires (NWs), including Yu-Shiba-Rusinov states, Andreev bound states (ABSs), and Majorana bound states [18, 20, 22–27].

The use of semiconductor-superconductor hybrids facilitates the realization of electrostatically controlled quantum dots (QDs) coupled to superconductors. QDs coupled to ABSs have received considerable attention from theoretical studies, including the use of the QD as a tool for measuring bound state lifetimes [28] or providing Majorana parity readout [21, 29–33]. In particular, the hybridization between a QD and a bound state leads to a shift of the bound state energy resulting in a characteristic ‘bowtie’ or ‘diamond’ shape. This can be used to determine the nonlocality and the spin structure of bound states [34–37].

In this Letter, we perform tunneling spectroscopy of a NW in a novel geometry that allows measurements at several side branches along the NW length using electrostatic gates patterned on an InAs/Al hybrid heterostructure. A similar configuration has been investigated theoretically [38], and a related experiment has been carried out in a conventional nanowire with deposited superconductor and normal metallic side contacts [39]. In addition to ABSs due to bound states in the NW, we find conductance resonances due to accidental QDs in the tunnel barriers. We investigate hybridization of QD states with ABSs in the NW, observing signatures of hybridization both locally, that is, at the position of the

accidental QD, and nonlocally, measured on another side probe away from the QD.

Figure 1(a) shows a micrograph of device 1, based on an InAs 2DEG with 5 nm of epitaxial Al. The device consists of an Al strip of width 100 nm and length 5 μ m, connected at both ends to large planes of Al that were electrically grounded. Gates labeled W_{kl} were Ti/Au on top of 30 nm HfO_2 , as shown in Fig. 1(e). Gates were used to deplete the semiconductor on either side of the Al wire, creating by depletion a quasi one-dimensional InAs NW self-aligned to the proximitizing Al.

Neighboring gates W_{kl} form a constriction that acts as a tunnel probe. The lead of the probe, away from the tunneling region, is made using the same unetched epitaxial Al. Tunneling across the bare semiconductor region between Al NW the Al lead is controlled by a probe gate, P_j , as shown in Fig. 1(f). Details of the materials and fabrication are given in the Supplementary Material.

The measurement set-up is shown schematically in Fig. 1(a). With the NW grounded, individual voltage biases $V_{\text{SD}}^{(j)}$ were applied on probe j via current to voltage converters. Tunneling currents I_j through the tunnel barriers were measured using lock-in detection yielding differential conductances $G_j = dI_j/dV_{\text{SD}}^{(j)}$. Measurements were carried out in a cryo-free dilution refrigerator with a 6-1-1 T vector magnet at ≈ 15 mK mixing-chamber temperature.

Tunneling conductances G_j as a function of magnetic field B_{\parallel} applied parallel to the NW are shown in Figs. 1(b-d). For weak tunneling and in the absence of probe resonances, G_j is proportional to the density of states in the NW. The superconducting gap of the Al in the leads of the probes closes at low field, $B_{\parallel} \approx 0.2$ T above which the probes can be regarded as normal metal, as discussed previously [16, 20]. The semiconductor under the Al in the NW was depleted by setting all W_{kl} gates to -4.5 V. Measurements on

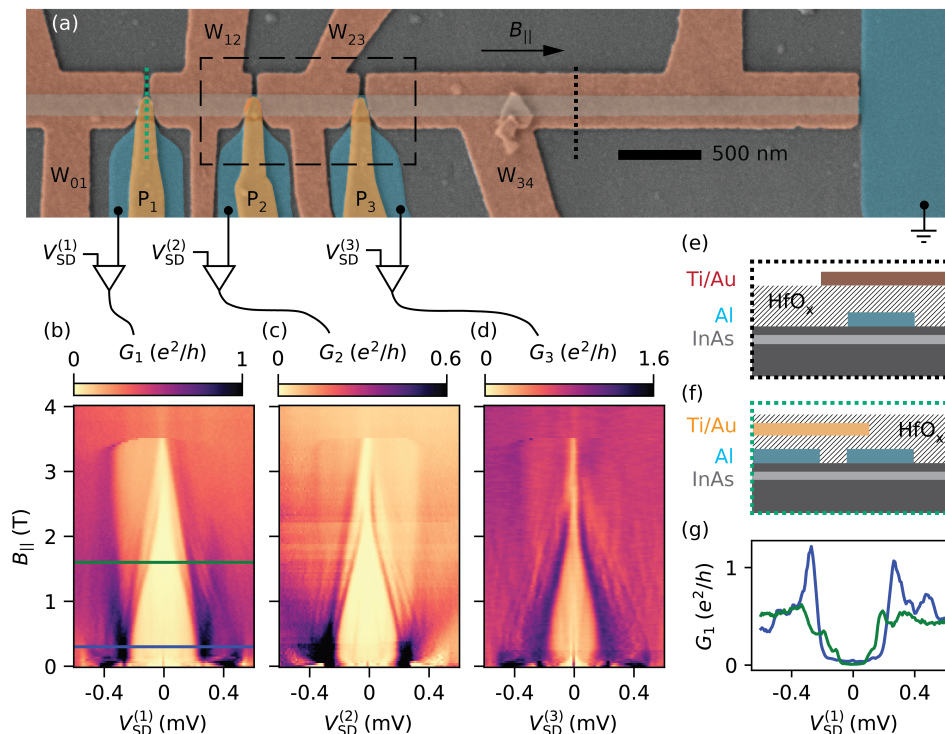


FIG. 1. (a) False colored scanning electron micrograph of device 1. The device consists of patterned epitaxial Al, forming a long narrow nanowire with several tunnel probes on top of an InAs quantum well. Gates labeled P_j are used to tune the tunnel barrier between the tunnel probe j and the wire ($j \in \{1, 2, 3\}$). Gates labeled W_{kl} with $kl \in \{01, 12, 23, 34\}$ deplete carriers except under the Al. (b-d) Tunneling spectroscopy at three probes with all gate voltages $V_{W_{kl}} = -4.5$ V. (e, f) Schematic cross sections of the device at the positions given by the green and black dotted lines in (a). (g) Line cuts at field values $B_{||} = 0.3$ T and $B_{||} = 1.6$ T indicated by the blue and green line in (b).

all three probes showed a superconducting gap closing without any subgap states crossing zero energy. For G_1 this is illustrated by the line cuts in Fig. 1(g). Note that the measurement of G_3 shows finite subgap conductance, which we attribute to probe 3 being tuned to an open regime with high-bias conductance $G_3(V_{SD}^{(3)} = 0.4 \text{ mV}) \gtrsim 1 e^2/h$.

To investigate the hybridization of a probe QD state with an ABS in the NW, we focus on the $0.6 \mu\text{m}$ long NW segment under gate W_{23} , see dashed box in Fig. 1(a), shown in Fig. 2(a). To create an ABS in this segment, the voltage on gate W_{23} was set less negative, in the range of -3 V, while voltages on neighboring gates W_{12} and W_{34} were set to -7.0 V. At $B_{||} = 1.6$ T and zero source drain biases, $V_{SD}^{(j)} = 0$, conductances G_2 and G_3 were measured as functions of probe-gate voltages V_{P_2} and V_{P_3} , respectively, and wire-gate voltage $V_{W_{23}}$. For both tunnel junctions, two sets of conductance resonances can be distinguished in Figs. 2(b) and (c) by their characteristic slope. The first set primarily consists of vertical features that are strongly dependent on the gate voltages V_{P_2} (V_{P_3}), which we attribute to QDs in the tunnel barriers. The second set are predominantly horizontal, depending more strongly on $V_{W_{23}}$. The latter resonances

are visible in both G_2 and G_3 , suggesting that they arise from ABSs that extend over the segment covered by gate W_{23} . Figure S1 in the Supplementary Material shows the complete evolution of tunneling spectroscopy from $V_{W_{23}} = -3.8$ V to $V_{W_{23}} = -3.0$ V while keeping the tunnel barriers at roughly constant transparency. This was achieved by compensating the effect of the gate W_{23} on the tunnel barriers by changing the gate voltages V_{P_2} , V_{P_3} given by the green dashed line in Figs. 2(b, c).

The blue star markers in Figs. 2(b, c) at gate voltages $V_{W_{23}} = -3.09$ V, $V_{P_2} = -0.045$ V, and $V_{P_3} = -0.170$ V mark ABSs that are weakly tunnel coupled to the probes. Tunneling spectroscopy of these ABSs as a function of magnetic field $B_{||}$ in Figs. 3(a, b) reveals a zero-bias crossing of the ABSs at $B_{||} = 1.6$ T followed by an overshoot at $B_{||} = 2$ T. The states appear in both tunneling conductance measurements of G_2 and G_3 . We extracted the peak position in $V_{SD}^{(2/3)}$ of the ABS from the measurements of G_2 and G_3 . The parametric plot of the peak positions $V_{SD}^{(2/3)}$ of the ABSs in G_2 and G_3 in Fig. 3(c) shows that all points lie close to the identity line, suggesting strong correlations. Details about the extraction of the peak position are outlined in the Supplementary Material.

The ABSs seen in G_2 and G_3 evolve similarly with

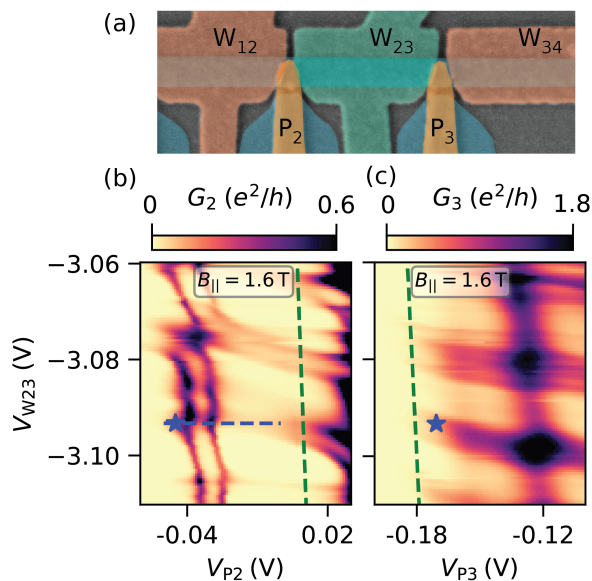


FIG. 2. (a) Micrograph of the NW segment under investigation. $V_{W12} = V_{W34} = -7.0$ V while the voltage on gate W_{23} (green), is varied. (b), (c) Differential conductance at zero bias measured at the left and the right end of the NW segment. Horizontal conductance resonances appear in both maps at similar gate voltages. Vertical conductance features, strongly dependent on gates V_{P2} and V_{P3} which tune the tunnel barriers, are also visible.

gate voltage V_{W23} and magnetic field $B_{||}$, suggesting that they belong to the same extended quantum states. Similar experimental findings have been made previously [40, 41]. The magnetic field dependence of the states is furthermore characteristic for ABSs in short NWs [27].

Special points in the measurement in Fig. 2(b) are the crossing points of the horizontal resonances with the sharp vertical resonances. At these points, an ABS in the NW is on resonance with the QD in the tunnel barrier under the gate P_2 . Tunneling spectroscopy G_2 using tunnel probe 2 at a field value of $B_{||} = 1.1$ T while sweeping V_{P2} along the values given by the blue dashed line in Fig. 2(b) is shown in Fig. 4(a). The ABSs were unaffected by the change of V_{P2} outside the range -0.040 V to -0.020 V. Within this range, the QD resonance appears as a conductance enhancement at high bias, reflecting the fact that G_2 was being measured through the QD in tunnel barrier 2. As the QD went on resonance with the ABSs, the ABSs with lowest energy merged at zero bias before returning to their previous energies. This resulted in a characteristic ‘bowtie’ shape of the resonances of the ABSs. A simultaneous measurement of G_3 during the sweep of V_{P2} at the other end of the NW is shown in Fig. 4(b). The enhancement of conductance at high bias due to the QD that was present in the measurement of G_2 was absent in the measurement of G_3 . The ABSs, however, showed the same ‘bowtie’ shape around the voltage value $V_{P2} \approx -0.030$ V which corresponds to

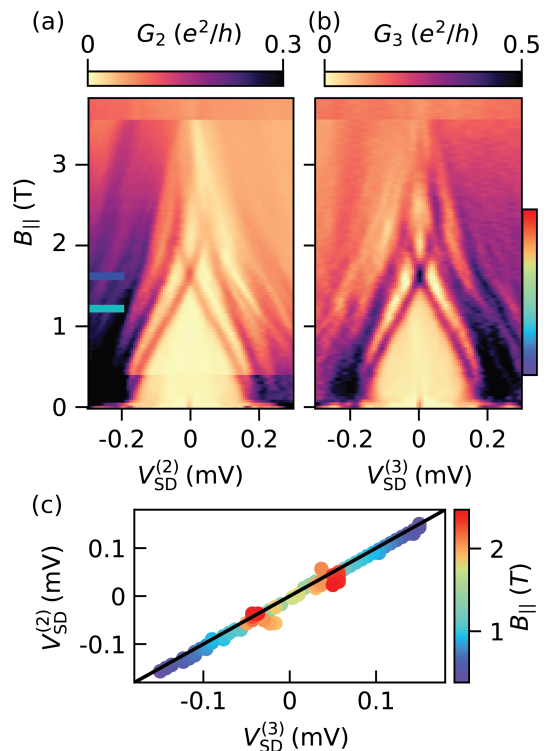


FIG. 3. (a, b) Tunneling spectroscopy with respect to magnetic field at the two ends of the NW with $V_{W23} = -3.09$ V [marked with \star on Fig. 2(b, c)]. Both measurements show subgap states crossing zero bias at $B_{||} = 1.6$ T with a clear overshoot around $B_{||} = 2$ T. (c) Parametric plot of the extracted peak positions from the lowest energy subgap states in (a) and (b). The color of the points indicates the field value in accordance with the rainbow color bar in (b).

the resonance condition between the ABSs and the QD in tunnel barrier 2. Note that in the measurement of both G_2 and G_3 not only the lowest energy ABSs undergo a change at the resonance condition with the QD, but also the higher excited states. In addition to the change in ABS energy, a clear change in the conductance peak height is visible when going through the resonance condition.

Around $B_{||} = 1.6$ T, the ABSs merged to yield a single conductance peak at zero bias. A measurement of G_2 with respect to V_{P2} in Fig. 4(c) shows that this peak was unperturbed except for voltage values around $V_{P2} \approx -0.030$ V where the QD was on resonance with the ABSs. At this point, the ABS resonances split symmetrically away from zero bias, forming a ‘diamond’ shape. The simultaneous measurement of G_3 in Fig. 4(d) reveals similar V_{P2} dependence of the ABS energy. Note that higher excited states were also affected around $V_{P2} \approx -0.030$ V.

The appearance of ABSs with ‘bowtie’- and ‘diamond’- shaped patterns while on resonance with the QD level is an indication of the QD being sufficiently tunnel coupled

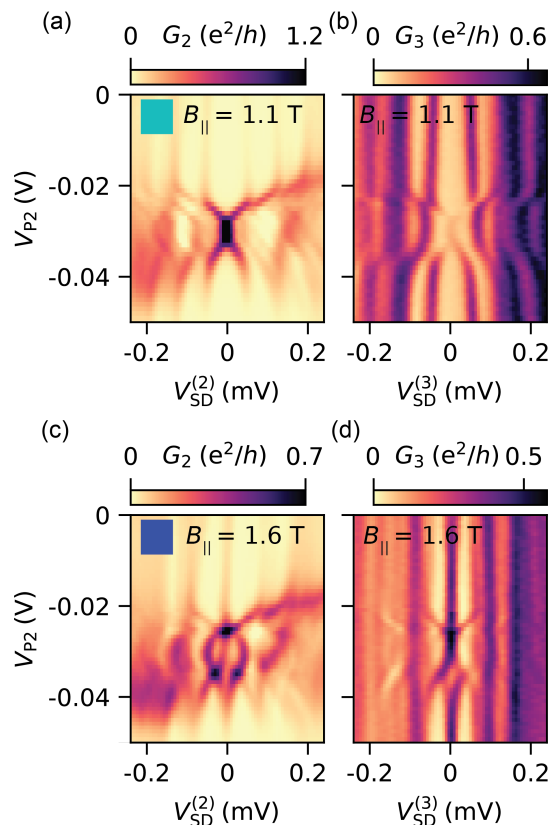


FIG. 4. (a) Tunneling conductance G_2 at the left side of the NW segment at $V_{W23} = -3.09$ V [marked with \star and blue dashed line on Fig. 2(b, c)] as a function of the gate voltage V_{P2} which tunes the tunnel barrier. A QD resonance is visible as an enhancement of conductance at high bias around $V_2 \approx -0.030$ V. The subgap states change their energy at the point of the QD resonance, drawing a characteristic ‘bowtie’ shape. (b) Tunneling spectroscopy G_3 at the other end of the NW. The ABS show the same change in energy as visible in the measurement of G_2 in (a). (c, d) same as (a, b) at higher parallel magnetic field, $B_{||}$. The ABSs split to form a ‘diamond’ shaped energy profile at the position of the QD resonance.

to the ABSs such that the two energy levels significantly hybridize, consistent with theoretical and previous experimental results [34–37, 42]. The measurement of the energy shift at both ends of the $0.6 \mu\text{m}$ NW, while a local

gate voltage at only one end is changed, is a nonlocal signature of the delocalized ABSs. If tunneling spectroscopy is measured at both ends of a NW, hybridization of bound states with a local QD can be used as a quantum mechanical tool to test whether a quantum state extends through the whole NW, similar to the analysis of cross-conductance and correlated appearance at both ends [40, 43]. This is in contrast to experiments where spectroscopy is performed at one end of a NW. In such a case, a QD in the absence of a bound states in the NW can mimic signatures of extended states inside the NW in tunneling spectroscopy [42, 44–48].

In comparison to previous experiments, the present set-up offers additional information about the spatial extent of the bound state, as one can perform tunneling spectroscopy at at both ends of the NW segment. This also allows for the observation of the change in energy of the ABS at one position while it is being hybridized with a QD $0.6 \mu\text{m}$ away by the means of changing a local gate. This nonlocal signature is a demonstration of the ABS being an extended quantum state.

In the Supplementary Material we present data of the hybridization of an ABS in the NW segment under the gate labeled W_{12} with a local QD in the tunnel barrier. Results from a second device (device 2) are also presented. Device 2 is a slightly different design, with side probes that do not have Al leads, only the bare semiconductor. Device 2 showed similar results as device 1 when an ABS in a NW was brought onto resonance with a QD localized at one probe while observing the impact of the hybridization on the bound state at the other probe.

ACKNOWLEDGMENTS

We thank Samuel Escribano, Karsten Flensberg, Max Geier, Andrea Maiani, Elsa Prada, Pablo San-Jose, and Waldemar Svejstrup for valuable discussions on theory, and Abhishek Banerjee, Lucas Casparis, Asbjørn Drachmann, Esteban Martinez, Felix Passmann, Daniel Sanchez, Saulius Vaitiekėnas, and Alexander Whiticar for input on experimental aspects. We acknowledge support from the Danish National Research Foundation, Microsoft, and a research grant (Project 43951) from VIL-LUM FONDEN.

- [1] P. Krogstrup, N. L. B. Ziino, W. Chang, S. M. Albrecht, M. H. Madsen, E. Johnson, J. Nygård, C. M. Marcus, and T. S. Jespersen, *Nat. Mater.* **14**, 400 (2015).
- [2] Y. Liu, S. Vaitiekėnas, S. Martí-Sánchez, C. Koch, S. Hart, Z. Cui, T. Kanne, S. A. Khan, R. Tanta, S. Upadhyay, M. E. Cachaza, C. M. Marcus, J. Arbiol, K. A. Moler, and P. Krogstrup, *Nano Lett.* **20**, 456 (2020).
- [3] F. Krizek, J. E. Sestoft, P. Aseev, S. Marti-Sanchez,

- S. Vaitiekėnas, L. Casparis, S. A. Khan, Y. Liu, T. Stankevič, A. M. Whiticar, A. Fursina, F. Boekhout, R. Koops, E. Uccelli, L. P. Kouwenhoven, C. M. Marcus, J. Arbiol, and P. Krogstrup, *Phys. Rev. Mater.* **2**, 093401 (2018).
- [4] V. M. Pereira, C.-N. Wu, K. Höfer, A. Choa, C.-A. Knight, J. Swanson, C. Becker, A. C. Komarek, A. D. Rata, S. Röbller, S. Wirth, M. Guo, M. Hong, J. Kwo, L. H. Tjeng, and S. G. Altendorf, *Phys. Status Solidi B*

- 258**, 2000346 (2021).
- [5] L. Fu and C. L. Kane, *Phys. Rev. Lett.* **100**, 096407 (2008).
- [6] L. Fu and C. L. Kane, *Phys. Rev. B* **79**, 161408 (2009).
- [7] X.-L. Qi, T. L. Hughes, and S.-C. Zhang, *Phys. Rev. B* **82**, 184516 (2010).
- [8] R. S. Mong, D. J. Clarke, J. Alicea, N. H. Lindner, P. Fendley, C. Nayak, Y. Oreg, A. Stern, E. Berg, K. Shtengel, and M. P. Fisher, *Phys. Rev. X* **4**, 011036 (2014).
- [9] O. Lesser, G. Shavit, and Y. Oreg, *Phys. Rev. Res.* **2**, 023254 (2020).
- [10] J. D. Sau, R. M. Lutchyn, S. Tewari, and S. Das Sarma, *Phys. Rev. Lett.* **104**, 040502 (2010).
- [11] A. Cook and M. Franz, *Phys. Rev. B* **84**, 201105 (2011).
- [12] R. M. Lutchyn, E. P. A. M. Bakkers, L. P. Kouwenhoven, P. Krogstrup, C. M. Marcus, and Y. Oreg, *Nature Reviews Materials* **3**, 52 (2018), 1707.04899.
- [13] D. J. Carrad, M. Bjergfelt, T. Kanne, M. Aagesen, F. Krizek, E. M. Fiordaliso, E. Johnson, J. Nygård, and T. S. Jespersen, *Advanced Materials* **32**, 1908411 (2020), 1911.00460.
- [14] J. O. Yuan, K. S. Wickramasinghe, W. M. Strickland, M. C. Dartiaill, K. Sardashti, M. Hatefipour, and J. Shabani, *Journal of Vacuum Science & Technology A* **39**, 033407 (2021), 2104.01159.
- [15] J. Shabani, M. Kjaergaard, H. J. Suominen, Y. Kim, F. Nichele, K. Pakrouski, T. Stankevic, R. M. Lutchyn, P. Krogstrup, R. Feidenhans'l, S. Kraemer, C. Nayak, M. Troyer, C. M. Marcus, and C. J. Palmstrøm, *Phys. Rev. B* **93**, 155402 (2016).
- [16] H. J. Suominen, M. Kjaergaard, A. R. Hamilton, J. Shabani, C. J. Palmstrøm, C. M. Marcus, and F. Nichele, *Phys. Rev. Lett.* **119**, 176805 (2017).
- [17] M. Kjaergaard, H. J. Suominen, M. P. Nowak, A. R. Akhmerov, J. Shabani, C. J. Palmstrøm, F. Nichele, and C. M. Marcus, *Phys. Rev. Appl.* **7**, 034029 (2017).
- [18] A. M. Whiticar, A. Fornieri, A. Banerjee, A. C. C. Drachmann, S. Gronin, G. C. Gardner, T. Lindemann, M. J. Manfra, and C. M. Marcus, *Phys. Rev. B* **103**, 245308 (2021).
- [19] E. C. T. O'Farrell, A. C. C. Drachmann, M. Hell, A. Fornieri, A. M. Whiticar, E. B. Hansen, S. Gronin, G. C. Gardner, C. Thomas, M. J. Manfra, K. Flensberg, C. M. Marcus, and F. Nichele, *Phys. Rev. Lett.* **121**, 256803 (2018).
- [20] F. Nichele, A. C. Drachmann, A. M. Whiticar, E. C. T. O'Farrell, H. J. Suominen, A. Fornieri, T. Wang, G. C. Gardner, C. Thomas, A. T. Hatke, P. Krogstrup, M. J. Manfra, K. Flensberg, and C. M. Marcus, *Phys. Rev. Lett.* **119**, 136803 (2017).
- [21] A. M. Whiticar, A. Fornieri, E. C. O'Farrell, A. C. Drachmann, T. Wang, C. Thomas, S. Gronin, R. Kallaher, G. C. Gardner, M. J. Manfra, C. M. Marcus, and F. Nichele, *Nat. Commun.* **11**, 1 (2020).
- [22] W. Chang, V. E. Manucharyan, T. S. Jespersen, J. Nygård, and C. M. Marcus, *Phys. Rev. Lett.* **110**, 217005 (2013).
- [23] A. Jellinggaard, K. Grove-Rasmussen, M. H. Madsen, and J. Nygård, *Phys. Rev. B* **94**, 064520 (2016).
- [24] E. J. H. Lee, X. Jiang, R. Žitko, R. Aguado, C. M. Lieber, and S. De Franceschi, *Phys. Rev. B* **95**, 180502 (2017).
- [25] J.-D. Pillet, C. H. L. Quay, P. Morfin, C. Bena, A. L. Yeyati, and P. Joyez, *Nat. Phys.* **6**, 965 (2010).
- [26] F. Nichele, E. Portolés, A. Fornieri, A. M. Whiticar, A. C. C. Drachmann, S. Gronin, T. Wang, G. C. Gardner, C. Thomas, A. T. Hatke, M. J. Manfra, and C. M. Marcus, *Phys. Rev. Lett.* **124**, 226801 (2020).
- [27] Y. Huang, H. Pan, C.-X. Liu, J. D. Sau, T. D. Stanescu, and S. Das Sarma, *Phys. Rev. B* **98**, 144511 (2018).
- [28] M. Leijnse and K. Flensberg, *Phys. Rev. B* **84**, 140501 (2011).
- [29] K. Gharavi, D. Hoving, and J. Baugh, *Phys. Rev. B* **94**, 155417 (2016).
- [30] S. Hoffman, C. Schrade, J. Klinovaja, and D. Loss, *Phys. Rev. B* **94**, 045316 (2016).
- [31] K. Flensberg, *Phys. Rev. Lett.* **106**, 090503 (2011).
- [32] M. Leijnse and K. Flensberg, *Phys. Rev. Lett.* **107**, 210502 (2011).
- [33] S. Plugge, A. Rasmussen, R. Egger, and K. Flensberg, *New J. Phys.* **19**, 012001 (2017).
- [34] D. J. Clarke, *Phys. Rev. B* **96**, 201109 (2017).
- [35] E. Prada, R. Aguado, and P. San-Jose, *Phys. Rev. B* **96**, 085418 (2017).
- [36] M.-T. Deng, S. Vaitiekėnas, E. Prada, P. San-Jose, J. Nygård, P. Krogstrup, R. Aguado, and C. M. Marcus, *Phys. Rev. B* **98**, 085125 (2018).
- [37] F. Peñaranda, R. Aguado, P. San-Jose, and E. Prada, *Phys. Rev. B* **98**, 235406 (2018).
- [38] T. D. Stanescu and S. Das Sarma, *Phys. Rev. B* **97**, 045410 (2018).
- [39] A. Grivnin, E. Bor, M. Heiblum, Y. Oreg, and H. Shtrikman, *Nat. Commun.* **10**, 1940 (2019).
- [40] G. L. R. Anselmetti, E. A. Martinez, G. C. Ménard, D. Puglia, F. K. Malinowski, J. S. Lee, S. Choi, M. Pendharkar, C. J. Palmstrøm, C. M. Marcus, L. Casparis, and A. P. Higginbotham, *Phys. Rev. B* **100**, 205412 (2019).
- [41] P. Yu, J. Chen, M. Gomanko, G. Badawy, E. P. A. M. Bakkers, K. Zuo, V. Mourik, and S. M. Frolov, *Nat. Phys.* **17**, 482 (2021).
- [42] A. Vuik, B. Nijholt, A. Akhmerov, and M. Wimmer, *SciPost Phys.* **7**, 061 (2019).
- [43] G. C. Ménard, G. L. R. Anselmetti, E. A. Martinez, D. Puglia, F. K. Malinowski, J. S. Lee, S. Choi, M. Pendharkar, C. J. Palmstrøm, K. Flensberg, C. M. Marcus, L. Casparis, and A. P. Higginbotham, *Phys. Rev. Lett.* **124**, 036802 (2020).
- [44] C.-X. Liu, J. D. Sau, T. D. Stanescu, and S. Das Sarma, *Phys. Rev. B* **96**, 075161 (2017).
- [45] E. J. H. Lee, X. Jiang, M. Houzet, R. Aguado, C. M. Lieber, and S. De Franceschi, *Nat. Nanotechnol.* **9**, 79 (2014).
- [46] M. Valentini, F. Peñaranda, A. Hofmann, M. Brauns, R. Hauschild, P. Krogstrup, P. San-Jose, E. Prada, R. Aguado, and G. Katsaros, *Science* **373**, 82 (2021).
- [47] C.-X. Liu, J. D. Sau, and S. Das Sarma, *Phys. Rev. B* **97**, 214502 (2018).
- [48] H. Pan and S. Das Sarma, *Phys. Rev. Res.* **2**, 013377 (2020).
- [49] Oxford Instruments, Triton 400.
- [50] Basel Precision Instruments SP983c.
- [51] Stanford Research Systems SR830, SR860.
- [52] M. T. Deng, S. Vaitiekėnas, E. B. Hansen, J. Danon, M. Leijnse, K. Flensberg, J. Nygård, P. Krogstrup, and C. M. Marcus, *Science* **354**, 1557 (2016).

SUPPLEMENTARY MATERIAL

Appendix A: Material, Fabrication, and Measurement Details

1. Wafer information

The material used for device 1 was an InGaAs/InAs/InAlAs heterostructure covered with an in-situ epitaxially grown Al top layer. Electron mobility in the InAs quantum well after removal of the Al by wet etching was measured using a Hall bar to be $25 \times 10^3 \text{ cm}^2 \text{ V}^{-1} \text{ s}^{-1}$. The material for device 2 was an InAlAs/InAs/InAlAs heterostructure with a similar epitaxial Al top layer.

2. Device Fabrication

Device fabrication was performed as follows: leads and bond pads were formed by wet etching a mesa structure defined by electron beam lithography (EBL). The wet etch was performed in two stages. First, the Al film was removed in the EBL patterned area using Transene aluminum etchant type D. Then, the semiconductor was etched $\sim 350 \text{ nm}$ deep using a solution of $\text{H}_2\text{O} : \text{C}_6\text{H}_8\text{O}_7 : \text{H}_3\text{PO}_4 : \text{H}_2\text{O}_2$ (220:55:3:3). Fine features (wire and probe leads) were patterned using a second EBL step. The Al film was again selectively wet etched using Transene aluminum etchant type D at 50°C . For device 1 a first layer of gate dielectric made of 15 nm HfO_x was grown globally on the chip using atomic layer deposition. The $5/20/5 \text{ nm}$ Ti/Au/Ti gates P_j were patterned by a third EBL step, followed by a metal deposition liftoff. Bond pads and connecting lines were fabricated in the same way with $10/350 \text{ nm}$ of Ti/Au. After a second global deposition of 15 nm HfO_x gate dielectric, the W_{kl} gates made from $5/20 \text{ nm}$ Ti/Au were deposited in a fifth EBL step. The corresponding bond pads, and connecting lines were fabricated from $10/350 \text{ nm}$ Ti/Au in a sixth EBL step, again using metal evaporation and liftoff. Note that P_j gates are buried inside dielectric. This way, narrow gates P_j can be fabricated that are close to the W_{kl} gates without risking a galvanic connections.

For device 2 only a single layer of 15 nm thick HfO_x was deposited using atomic layer deposition. All gates made from $5/20 \text{ nm}$ thick Ti/Au were fabricated using EBL, metal deposition, and liftoff. The bond pads and connecting lines to the gates were fabricated the same way from $10/350 \text{ nm}$ thick Ti/Au.

3. Measurement setup

A schematic of the experimental set-up for transport measurements is depicted in Fig. S1. The sample was mounted in a puck-loading cryo-free dilution refrigerator [49] equipped with a 6-1-1 T vector magnet. Throughout the measurements, the mixing chamber of the dilution fridge was at base temperature of roughly 15 mK , without active control, as measured by a RuO_2 -based thermometer. Gate voltages were generated using an in-house built digital-to-analog converter with 20-bit precision. The three tunneling currents I_j were amplified using a current-to-voltage converter [50] followed by an AC lock-in amplifier [51]. Bias voltages $V_{\text{SD}}^{(j)}$ were applied via the offset voltage inputs of the current-to-voltage converters. The DC component of $V_{\text{SD}}^{(j)}$ was supplied by the digital-to-analog (D/A) converter and an additional AC component $dV_{\text{SD}}^{(j)}$ at a frequency f_j was supplied by the sine output of lock-in amplifier j . The frequencies were $f_1 = 42.2 \text{ Hz}$, $f_2 = 31.9 \text{ Hz}$, $f_3 = 20.4 \text{ Hz}$. In-house built multi-stage low-pass filters at the mixing chamber plate were used to attenuate electrical noise. The two ground planes of Al that connect to the nanowire (NW) at both ends were connected via two lines each to ground at the breakout box.

For measurements in Figs. 1(b-d) in the main text, the DC bias voltage was swept simultaneously for all three tunnel probes, i.e., $V_{\text{SD}}^{(1)} = V_{\text{SD}}^{(2)} = V_{\text{SD}}^{(3)}$. For all other tunneling spectroscopy measurements, where only two conductances are reported, the third probe was left floating. The two bias voltages were swept sequentially, with the respective other set to zero.

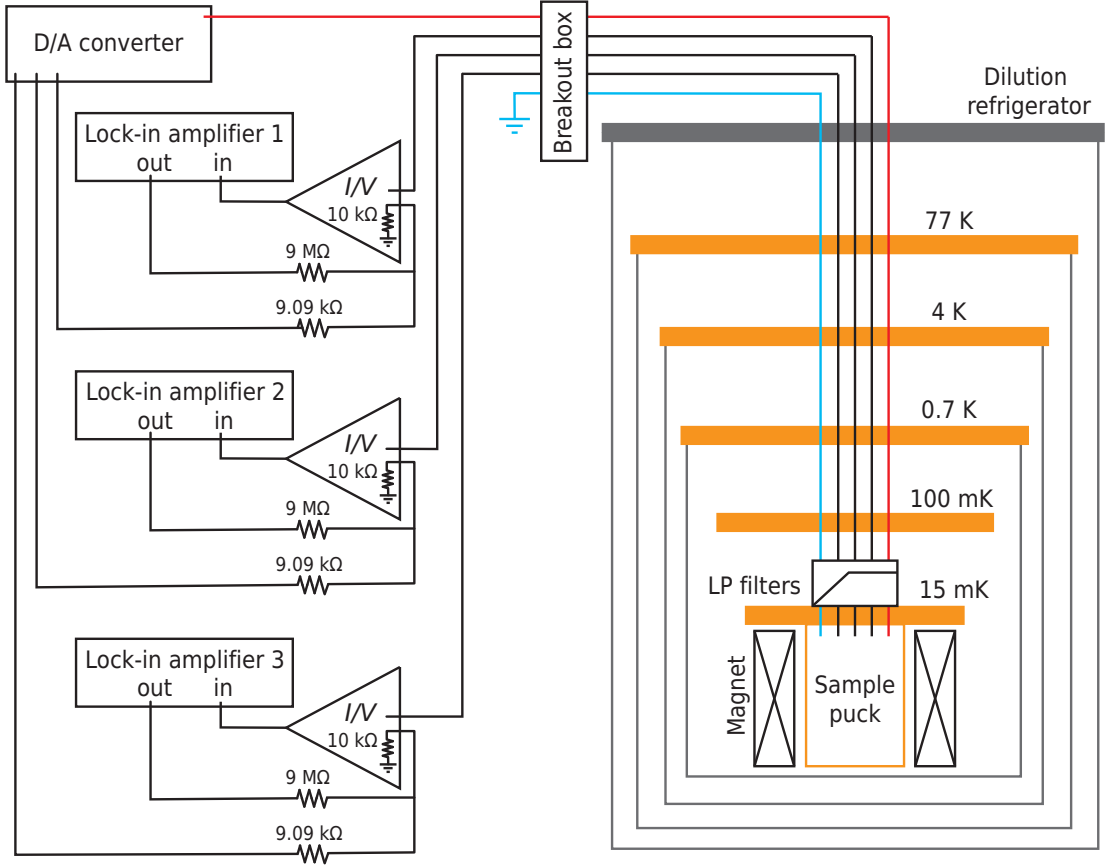


FIG. S1. Schematic overview of the experimental measurement setup. All lines that supply gate voltages are pictured by the red line. The four lines that are used to connect the ground planes of the sample to the breakout box are represented by a single blue line. The dilution refrigerator is an Oxford Instruments Triton 400. The three current-to-voltage (I/V) converting amplifiers are made by Basel Precision Instruments (part number SP983c). Source-drain bias voltage is supplied to the sample via the input voltage offset port of the I/V converters. Suitable resistors together with the input resistance of this port form a voltage divider. The lock-in amplifiers are made by Stanford Research Systems (model SR830 and SR860).

Appendix B: Additional data, device 1

1. W_{23} dependence of subgap states

The data shown in the following was measured on device 1 and provides additional information to the discussion in the main text. Figures S2(a,b) show the evolution of G_2 and G_3 from $V_{W23} = -3.8$ V to $V_{W23} = -3.1$ V at $B_{||} = 1.6$ T. Note that while changing V_{W23} , the voltages V_{P2} and V_{P3} were changed according to the relations

$$\begin{aligned} V_{P2} &= -10 \text{ mV} - \frac{0.05}{0.40} \cdot (V_{W23} + 3.1 \text{ V}) \\ V_{P3} &= -135 \text{ mV} - \frac{0.045}{0.40} \cdot (V_{W23} + 3.5 \text{ V}) \end{aligned} \quad (\text{S1})$$

The lines given by these relations are shown in green in Figs.2(b, c) of the main text. This compensates for the effect of the gate V_{W23} on the tunnel barriers and ensures that the high bias conductance stays around $\sim 0.1 e^2/h$ throughout the complete range of $-3.8 \text{ V} < V_{W23} < -3.1 \text{ V}$. To denote that more than one gate voltage was changed during the measurement, we label the variable \tilde{V}_{W23} instead of V_{W23} . There are no states crossing zero bias for voltage values $\tilde{V}_{W23} < -3.3$ V. Above that value Andreev bound states (ABSs) cross the gap. Line cuts at zero bias are displayed in Fig. S2(c). A measurement with higher resolution within the range $-3.06 \text{ V} < \tilde{V}_{W23} < -3.12 \text{ V}$ in Figs. S2(d, e)

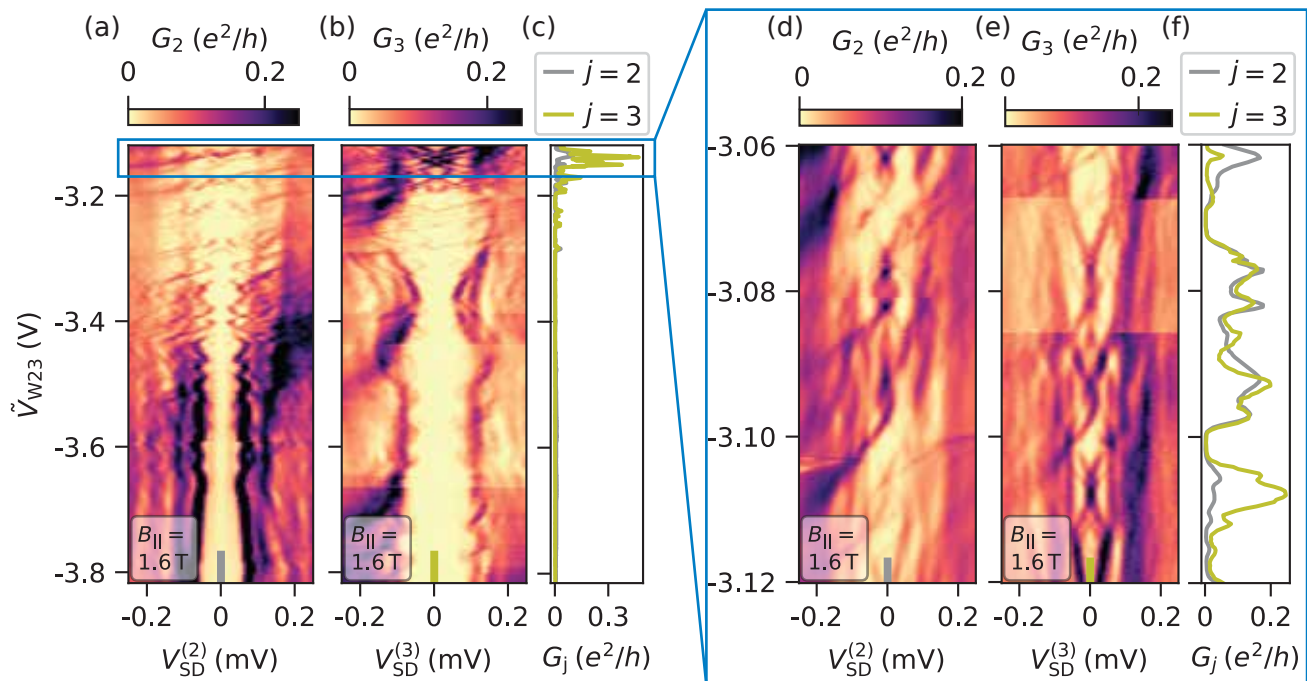


FIG. S2. (a, b) show conductance spectroscopy measurements of G_2 and G_3 over a wide range of V_{W23} . The voltages on the tunnel barrier gates V_{P2} and V_{P3} were compensated according to Eqs. S1. The variable on the vertical axis is therefore marked \tilde{V}_{W23} instead of V_{W23} . No subgap state crosses zero bias for gate voltages $\tilde{V}_{W23} < -3.3$ V. A line cut at zero bias for G_2 and G_3 is plotted in (c). A zoomed-in measurement of G_2 and G_3 is depicted in (d) and (e). It reveals subgap states whose peak positions show identical nontrivial gate voltage dependence in both G_2 and G_3 . The data for G_2 and G_3 at zero bias is plotted in (f) for comparison.

shows that subgap states evolve with the same nontrivial dependence on \tilde{V}_{W23} in measurements of G_2 and G_3 . At the same time, the subgap states can appear with different strength in conductance in G_2 and G_3 . A line cut taken at zero bias in Fig. S2(f) shows the correlated \tilde{V}_{W23} dependence on both sides in the form of coinciding peak positions, while the difference in conductance value by up to one order of magnitude for some of the subgap states is apparent from the difference in peak height.

2. Extraction of peak positions

We extracted peak positions of subgap states from G_2 and G_3 as functions of magnetic field and $V_{SD}^{(2)}$ and $V_{SD}^{(3)}$ used in Figs. 3(b, c) in the main text as follows: local maxima of $G_{(2/3)}$ were found for each value of B_{\parallel} within the range $0.38 \text{ T} < B_{\parallel} < 2.5 \text{ T}$, wherever the subgap state is resolved. Detected peaks are marked in the measurements of G_2 and G_3 in Figs. S3(a, b). As a next step, the maxima that are obviously (by eye) not arising from the subgap state of interest but due to noise or higher excited states are discarded. The same applies for values of B_{\parallel} at which only one subgap peak could be detected in one of the two measurements, while other measurement showed two peaks. These post-selected peak positions associated with the subgap state of interest are plotted in Fig. S3(c).

3. No nonlocal signature in the absence of Andreev bound states

In the case of a rather negative gate voltage V_{W23} around -4 V we observed no subgap state that appears in both G_2 and G_3 , while the quantum dot (QD) resonance in the tunnel barrier under P_2 was still present. In this configuration, no nonlocal signatures can be measured in tunneling spectroscopy.

Tunneling spectroscopy in Figs. S4(a, b) shows no subgap states crossing zero bias. A measurement of tunneling spectroscopy in a small range around $\tilde{V}_{W23} = -3.93$ V at $B_{\parallel} = 1.6$ T in Figs. S4(c, d) shows a gap with no subgap states persisting over the whole range of V_{W23} . In Fig. S4(e) tunneling spectroscopy as a function of the gate voltage

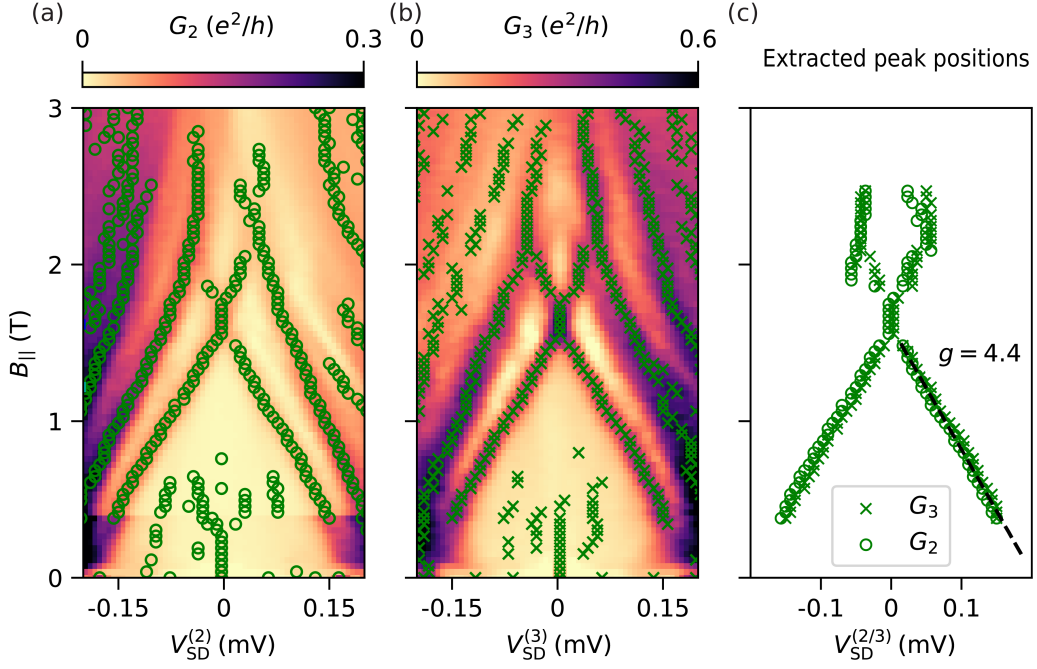


FIG. S3. (a, b) Identical data to the ones in Figs. 3(a, b) in the main text. The green markers indicate the position of identified local maxima for individual magnetic field values. They originate from subgap states, noise, and a supercurrent peak at low magnetic field values. (c) Locations of the local maxima from (a) and (b) after removing the peaks that we identify not to stem from the low energy subgap states of interest.

V_{P2} reveals the QD resonance around $V_{P2} = 0.01$ V at high bias [18, 22, 23, 45]. The measurement of G_3 while sweeping V_{P2} over the QD resonance is shown in Fig. S4. Throughout the measurement, G_3 is independent of V_{P2} , in particular around the value $V_{P2} = 0.01$ V at which the QD resonance appears in G_2 .

In summary, in the absence of a discrete subgap state extending between the two probes, no change in the density of states is measured on one probe while a QD on the other tunnel probe is brought on resonance. This shows that only an extended ABS can hybridize with a local QD and lead to a measurable nonlocal signature on a tunnel probe 0.6 μm away from the QD.

Appendix C: Supplementary data on device 1 - Andreev bound states under W_{12}

In the main text, data of the hybridization between an ABS in the NW segment under the gate W_{23} and a local QD is shown. Here data of the comparable experiment with an ABS in the NW segment under the gate W_{12} , which is marked green in Fig. S9(a), is presented.

The gate voltage dependence of conductance resonances with respect to the voltages on the gate V_{W12} that covers the NW and the two gates P_1 and P_2 , while keeping the neighboring gate voltages at $V_{W01} = V_{W23} = -4.5$ V can be seen in Fig. S5(c,d). There are horizontal resonances in G_2 and G_3 that are associated with extended states in the NW. In addition vertical resonances, which can be attributed to localized states in the respective tunnel barrier regions, are present.

Tunneling spectroscopy data as a function of V_{W12} , using tunnel probes 1 and 2, are shown in Figs. S6(a,b). Voltages on the gates P_1 and P_2 were compensated according to:

$$\begin{aligned} V_{P1} &= -307 \text{ mV} - \frac{0.01}{0.80} \cdot (V_{W12} + 3 \text{ V}) \\ V_{P2} &= -15 \text{ mV} - \frac{0.015}{0.80} \cdot (V_{W12} + 3 \text{ V}). \end{aligned} \quad (\text{S1})$$

To denote that more than one gate voltage was changed during the measurement, the variable is labeled \tilde{V}_{W12} instead of V_{W12} . Tunneling conductances G_1 and G_2 in Figs. S6(a, b) show subgap states as a function of \tilde{V}_{W12} . These states

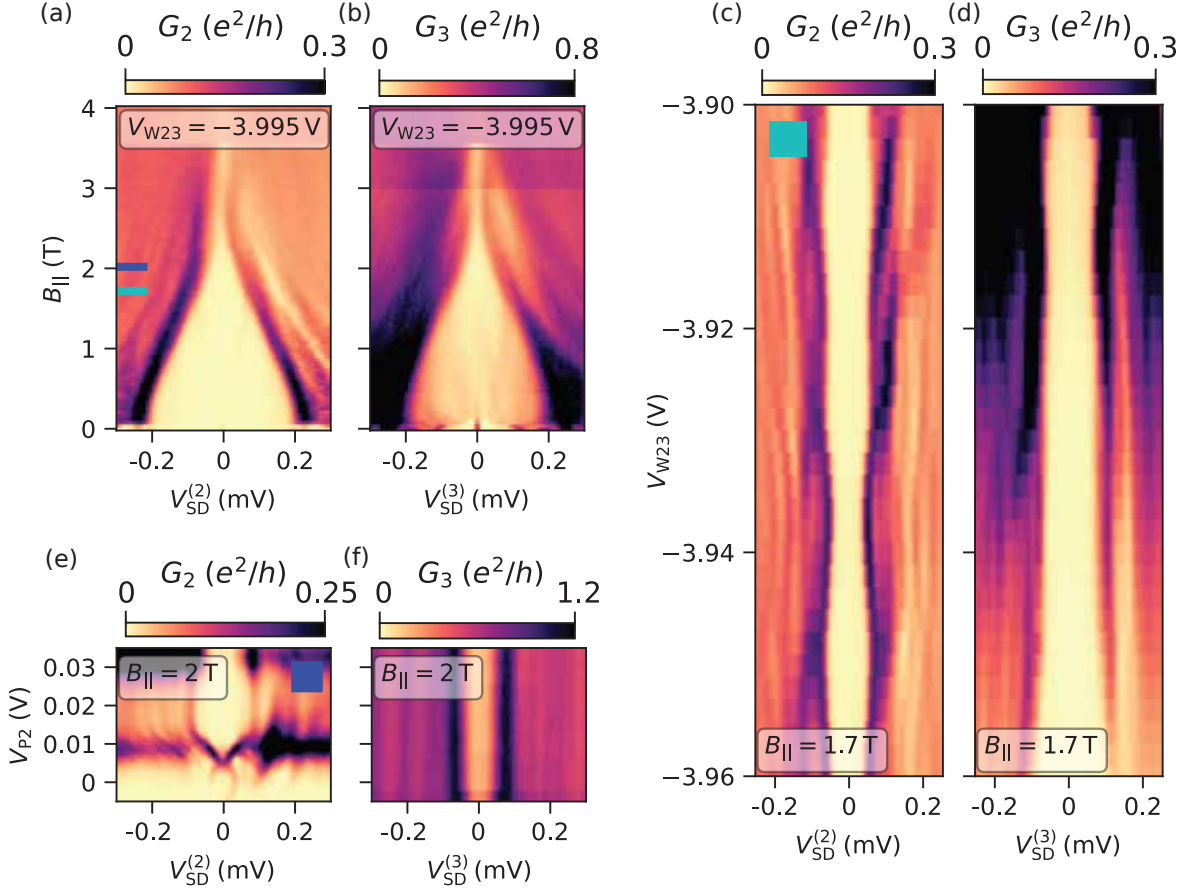


FIG. S4. (a) and (b) show tunneling spectroscopy data of G_2 and G_3 with $V_{W12} = V_{W34} = -7$ V and $V_{W23} = -3.995$ V. There is no subgap state visible. Tunneling spectroscopy with respect to changing gate voltage V_{W23} at $B_{||} = 1.7$ T is plotted in (c) and (d). There is no subgap state present. Tunneling conductance measurement with respect to the gate voltage V_{P2} that tunes the tunnel barrier is depicted in (e) and (f). While G_2 shows a clear subgap state at the position of the QD resonance, the data of G_3 in (f) shows no measurable change at the same gate voltage.

show similar dependences on \tilde{V}_{W12} in the two measurements. This is emphasized by the line cut taken at zero bias in Fig. S6(c).

Tunneling conductance as a function of magnetic field $B_{||}$ is shown in Fig. S7(a, b). Subgap states were found to emerge at low magnetic field from the quasiparticle continuum. At $B_{||} = 1.6$ T, subgap states cross zero bias and overshoot at $B_{||} = 2$ T. For every value of $B_{||}$ we extracted the peak position from the measured trace of G_1 (G_2) according to the procedure outlined in B2. Extracted peak positions are shown in Fig. S10(d). The same peak positions are plotted parametrically in Fig. S10(c). In the parametric plot, all points lie on or close to the identity line demonstrating the similar behavior of the subgap states in measurements of G_1 and G_2 . Due to their correlated behavior in G_1 and G_2 with respect to magnetic field and V_{W12} gate voltage, we attribute these subgap states to ABSs that extend over the NW segment under gate V_{W12} .

To investigate the effect on the subgap states as the ABS is brought on resonance with the QD in the tunnel barrier under P_2 , we performed tunneling spectroscopy with respect to the voltage on gate P_2 . The measurement of G_1 and G_2 at $B_{||} = 1.1$ T is plotted in Figs. S8(a) and (b). A QD resonance can be seen around $V_{P2} = -0.02$ V as signal enhancement at high bias in the measurement of G_2 . In the vicinity of the QD resonance, the subgap states exhibit a ‘bowtie’ shape with a conductance enhancement at the point where the states cross zero bias in G_2 . The simultaneous measurement of tunneling conductance G_1 shows that the subgap states are almost constant in energy, up to a small region around $V_{P2} \sim -0.02$ V around the QD resonance. In the vicinity of the QD resonance, the lowest energy subgap state decreases in intensity in G_1 such that it is not visible at the position of the QD resonance.

A measurement of the same type at a higher magnetic field value of $B_{||} = 1.6$ T is shown in Figs. S8(c) and (d). The quantity G_2 , which is measured through the QD, shows the QD resonance crossing the gap at $V_{P2} = -0.02$ V. A

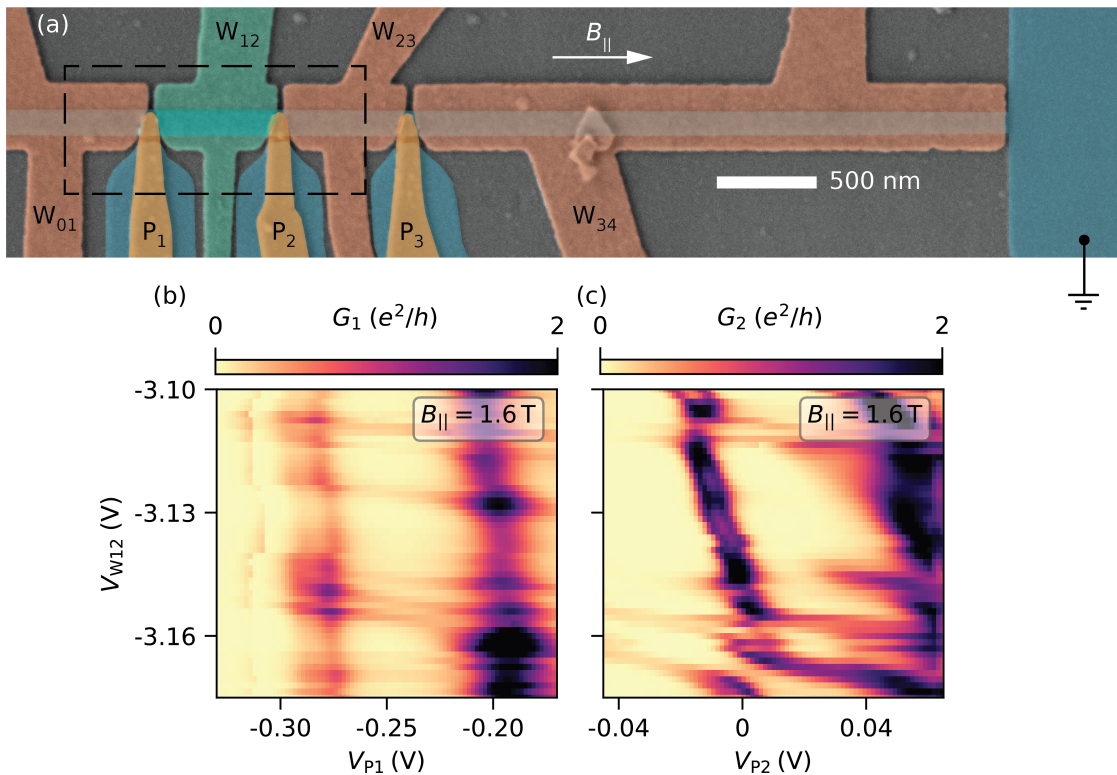


FIG. S5. (a) False-color scanning electron micrograph of device 1. (b) and (c) show conductance resonances measured at $B_{||} = 1.6$ T at $V_{SD}^{(j)} = 0$ V. Both measurements show two distinct families of states - horizontal ones, that strongly depend on V_{W23} , and vertical ones, that strongly depend on the gate voltage that tunes the respective tunnel barrier.

similar pattern to the one shown in Fig. 4(c) in the main text is visible around zero bias at the point where the QD is on resonance with the subgap state close to zero bias. The resolution is not sufficient to resolve the exact pattern and determine whether the subgap states shift in energy around the QD resonance to form a ‘diamond’ shape. The measurement of G_1 shows that the conductance value measured for the subgap state at zero bias decreases abruptly around the QD resonance while a splitting of the states away from zero energy is resolved.

For all measurements in Fig. S8 a clear effect on the ABSs can be observed at tunnel barrier 1 when the subgap state is brought on resonance with a QD in tunnel barrier 2, even though the precise line shape of the subgap state is not resolved in this measurement. The change in conductance value of the subgap state at the point of the QD at both ends is stronger in this measurement compared to the data presented in the main text.

Appendix D: Device 2

We fabricated a second device with semiconducting, instead of superconducting, side probes, i.e. with the epitaxial Al removed in the leads of the side probes. The device is depicted in Fig. S9(a). It consists of a superconducting strip of Al on top of an InAs quantum well. The gates labeled T_{kl} are used to electrostatically define the NW on one side and tune the electron density of individual segments of the NW. The gates labeled B_{kl} serve the purpose of defining the wire on the other side, tuning its electron density, and forming a quantum point contact between adjacent B_{kl} gates. The gates P_1 and P_2 add additional control over the quantum point contacts. In the data presented in the following, the gate voltages $V_{T01} = V_{T23} = -6$ V, $V_{B01} = V_{B23} = -2.4$ V, $V_{B12} = -2.5$ V were kept at fixed values.

Measurements of conductance resonances in G_1 (G_2) at zero bias and magnetic field $B = 0.8$ T with respect to the gate voltages V_{T12} and V_{P1} (V_{P2}) are shown in Figs. S9(c) and (d). Both measurements reveal resonances that strongly depend on V_{T12} originating from states inside the NW. The measurement of G_2 furthermore shows two resonances that strongly couple to the gate voltage V_{P2} . These features can be associated with a QD in the tunnel barrier, which is verified by bias spectroscopy shown in Fig. S9(b). The conductance shows a Coulomb diamond at high bias as

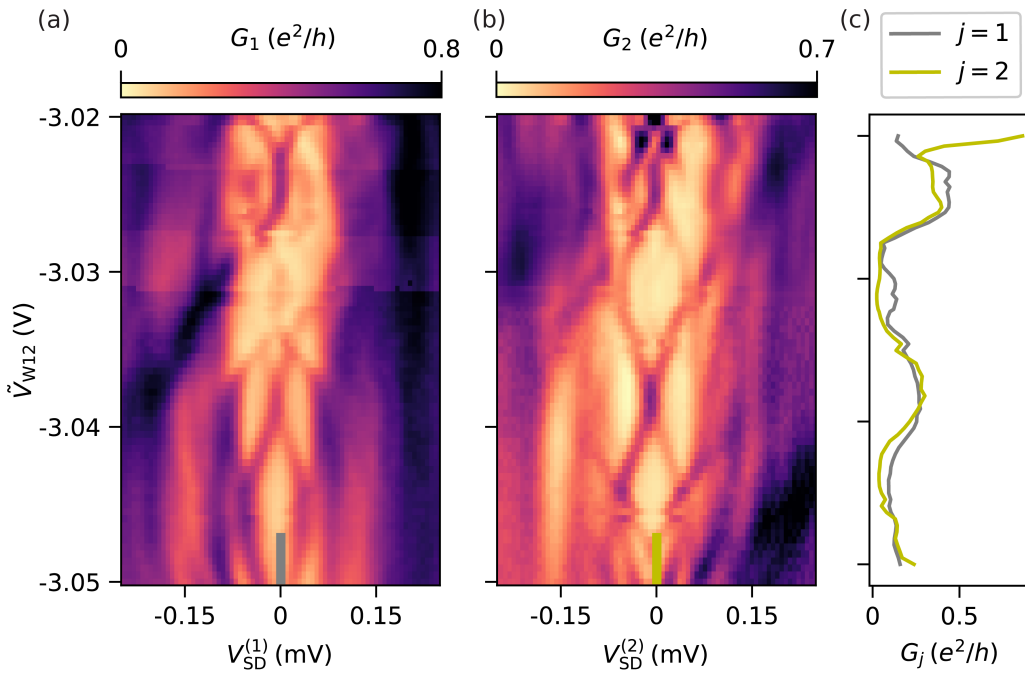


FIG. S6. (a, b) Tunneling spectroscopy measurements of G_2 , G_3 with respect to \tilde{V}_{W12} . The voltages on the other gates were fixed at $V_{W01} = V_{W23} = V_{W34} = -4.5$ V. Subgap states appear in both measurements of G_1 and G_2 . The data for G_2 and G_3 at $V_{SD}^{(1)} = V_{SD}^{(2)} = 0$ V is plotted in (c) for comparison.

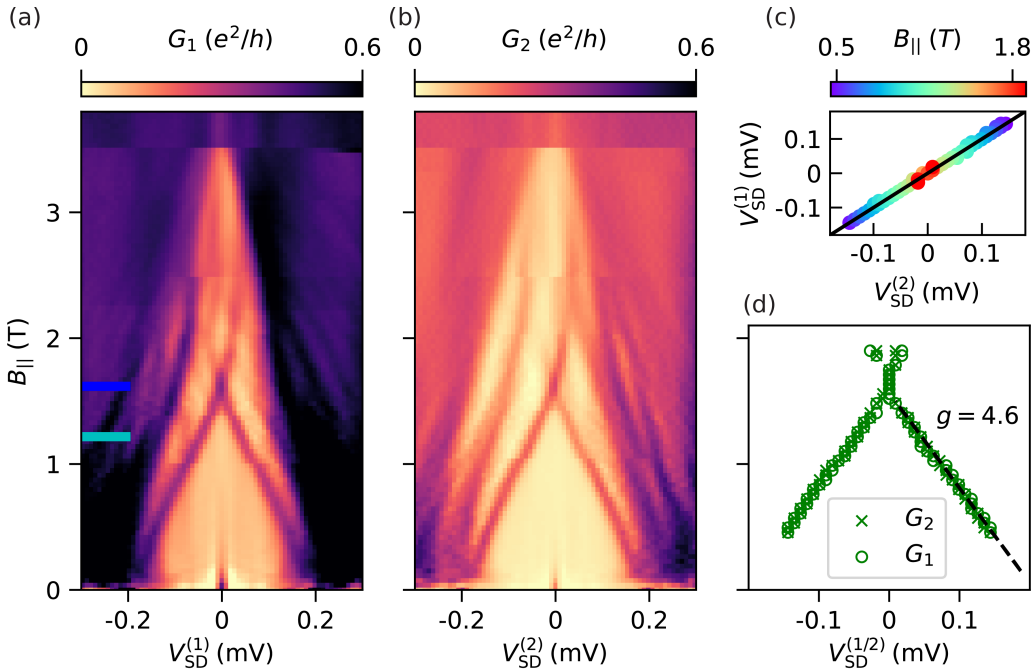


FIG. S7. (a, b) Tunneling spectroscopy measurements G_1 , G_2 with respect to magnetic field $B_{||}$ at $V_{W12} = -3.02$ V. The peak positions that were extracted according to the procedure described in section B2 are plotted in (d). A parametric plot of the same data points as in (d) is shown in (c).

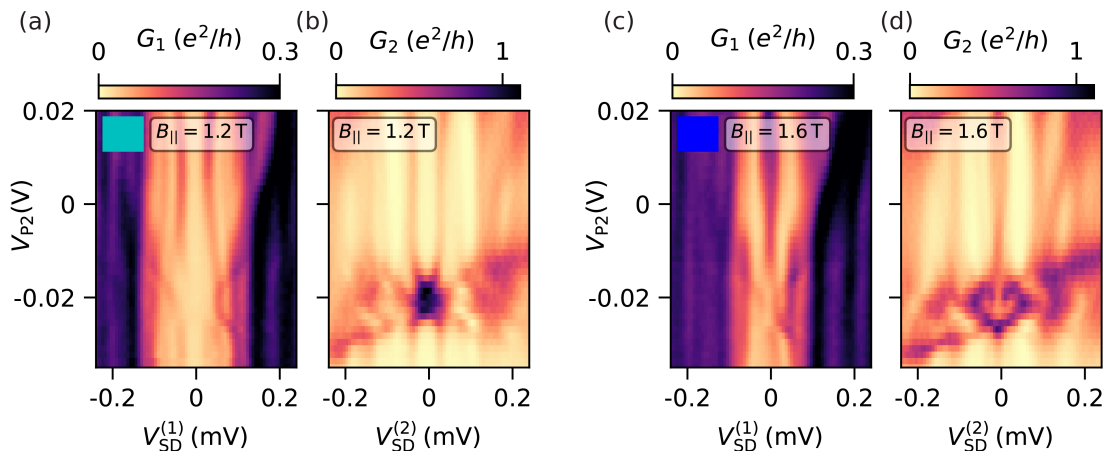


FIG. S8. Tunneling spectroscopy data at $V_{W12} = -3.02$ V as a function of gate voltage V_{P2} is plotted in (a) and (b). A QD resonance is clearly visible in the measurement of G_2 . The same measurement at higher magnetic field $B_{||} = 1.6$ T is shown in (c) and (d).

emphasized by the cyan, dashed lines. This allows for an estimate of the charging energy to be ~ 1 meV.

Tunneling spectroscopy measurements of subgap states in G_1 and G_2 at $B_{||} = 1.1$ T are shown in Fig. S9(e) and (f). The gate voltages $V_{P1} = 0.22$ V and $V_{P2} = 0.05$ V were kept constant during this measurement, which corresponds to the green dashed lines in Fig. S9(c, d). Similar to the results of device 1, states appear in both measurements of G_1 and G_2 with the same nontrivial dependence on the voltage V_{T12} . The conductance value with which states appear in the two measurements can be very different, however. A line cut at zero bias is depicted in Fig. S9(g) and captures the correlated dependence of conductance peaks with respect to V_{T12} in the form of concomitant peak positions. The difference in conductance values results in a difference in peak heights for the two different curves in Fig. S9(g).

Figures S10(a, b) show tunneling spectroscopy data of G_1 and G_2 for device 2 as a function of magnetic field $B_{||}$ parallel to the NW. The induced gap at low field given by the lowest energy states is ~ 80 μ eV. Note that this device was fabricated on material where the InAs quantum well is separated by an InAlAs barrier from the superconducting Al.

The lowest energy states in both G_1 and G_2 cross zero bias at around $B_{||} = 1.5$ T. Extracting the peak positions for each value of $B_{||}$ and plotting them parametrically reveals strong correlation as shown in Fig. S10(c). Based on this strong correlation in G_1 and G_2 with respect to magnetic field and V_{T12} , we attribute these subgap states to extended ABSs in the NW.

To investigate the behavior around places where the ABSs in the NW are on resonance with the QD in tunnel barrier 2, we measured tunneling spectroscopy with respect to V_{P2} . While sweeping V_{P2} , the gate voltage V_{T12} was compensated to mitigate the effect that V_{P2} has on the ABSs inside the NW. The parametric equation that was used is given by

$$V_{T12} = -4.664 \text{ V} - \frac{0.014}{0.18} \cdot (V_{P2} + 0.08 \text{ V}) \quad (\text{S1})$$

and is depicted by the blue dashed line in Fig. S9(d). To denote that more than one gate voltage was changed during the measurement, the variable is labeled \tilde{V}_{P2} instead of V_{P2} . The measured tunneling spectroscopy G_1 and G_2 is depicted in Fig. S11(a) and (b) for a magnetic field value of $B_{||} = 0.5$ T. The lowest energy subgap states in G_2 show a clear crossing at zero energy with the characteristic ‘bowtie’ shape at the location of the QD resonance at $\tilde{V}_{P2} = -0.02$ V. The states at higher bias are not well resolved in the measurement of G_2 . The lowest energy subgap states in G_1 show a ‘bowtie’ shape in the form of a zero bias crossing at the location of the QD resonance. For the measurement of G_1 , the higher excited states are well resolved and a shift in energy for all higher excited states is visible at the position of the QD resonance.

Identical measurements of G_1 and G_2 at a higher magnetic field, $B_{||} = 0.8$ T, are depicted in Figs. S11(c, d). At the point of the QD resonance all conductance resonances shift in energy. The pair of subgap states with lowest energy merge from two separated peaks at $\tilde{V}_{P2} > -0.02$ V to a single peak at zero bias for $\tilde{V}_{P2} < -0.02$ V. This pattern shows close similarity to the results presented in Ref. [52].

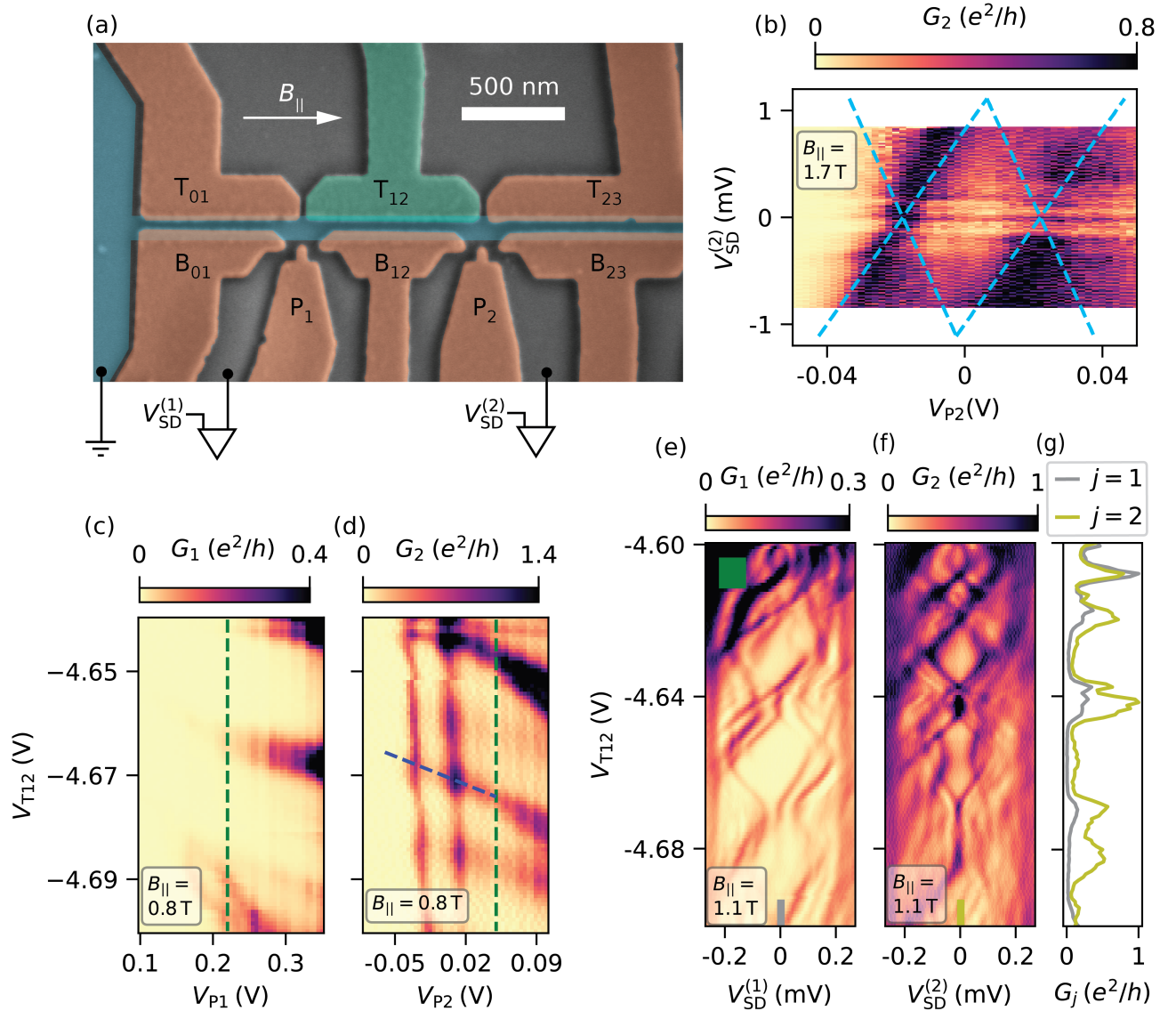


FIG. S9. (a) False-color scanning electron micrograph of device 2. The device consists of a superconducting Al NW on top of a InAs quantum well. The gates labeled V_{P_j} can be used to tune the tunnel barrier between the tunnel probe j and the wire ($j \in \{1, 2, 3\}$). The gates labeled $V_{B_{kl}}$ form the confining potential of the quasi one-dimensional NW at the bottom edge while also forming tunnel barriers. The gates labeled T_{kl} confine the NW at the top edge and tune the chemical potential of individual NW segments ($kl \in \{01, 12, 23\}$). (c, d) Tunneling conductance measurements of G_1 , G_2 with $V_{SD}^{(j)} = 0$ V. States that couple strongly to the gate voltage V_{TI12} are visible in both measurements. Two sharp resonances that strongly depend on the gate voltage V_{P2} appear in the measurement of G_2 . (b) Tunneling spectroscopy at $V_{TI12} = -4.67$ V. The dashed lines serve as a guide to the eye. Tunneling spectroscopy at $B_{||} = 1.1$ T, when moving the gate voltages along the green dashed lines at $V_{P1} = 0.22$ V and at $V_{P2} = 0.05$ V in (c, d) are plotted in (e, f). While the absolute values of tunneling conductance in G_1 and G_2 are different, the structure of the states in energy is nearly identical. A line cut at $V_{SD}^{(1)} = V_{SD}^{(2)} = 0$ V of the data in (e, f) is shown in (g).

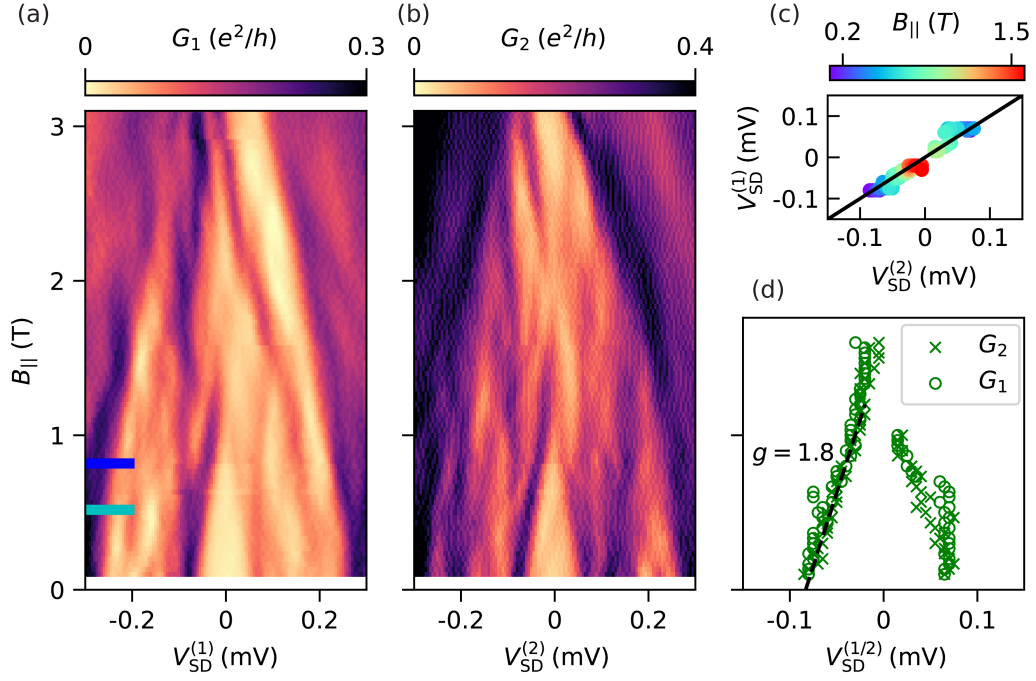


FIG. S10. (a,b) Tunneling spectroscopy with respect to magnetic field $B_{||}$ with $V_{T12} = -4.67$ V. The induced gap at zero field is ~ 80 μ eV. Peak positions extracted from G_1 and G_2 associated with the lowest energy state are plotted in (d). (c) Parametric plot of the peak positions from (d).

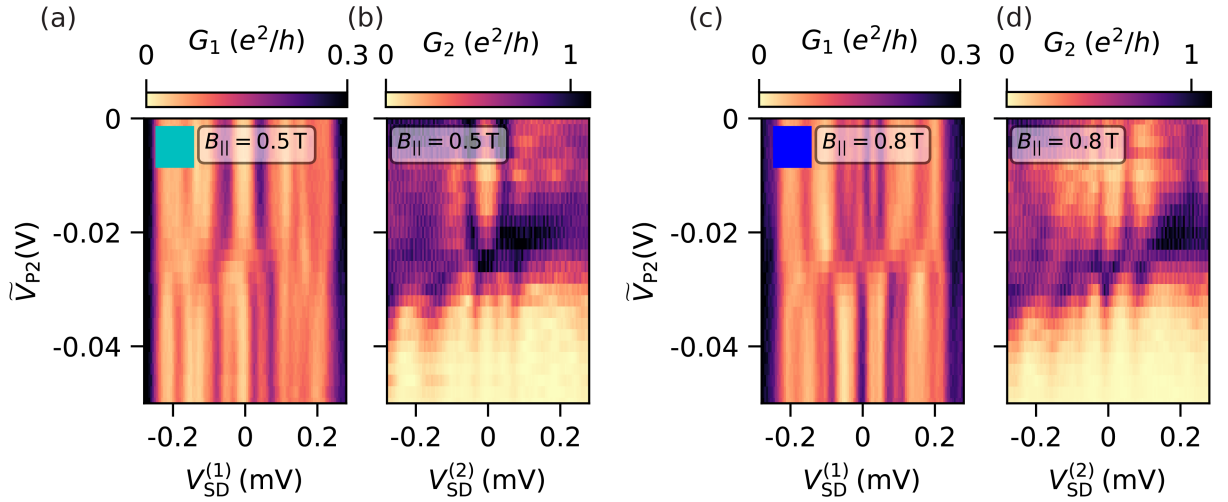


FIG. S11. (a, b) Tunneling conductance measured while changing the gate voltages V_{P2} and V_{T12} along the blue dashed line according to equation S1. To indicate that more than one gate voltage was changed, the variable on the vertical axes is labeled \tilde{V}_{P2} instead of V_{P2} . At $\tilde{V}_{P2} = -0.025$ V a QD resonance is visible in G_2 . In both G_1 and G_2 , the subgap states draw a ‘bowtie’ shape at this value of gate voltage. (c, d) The same measurement as in (a, b) but at a higher magnetic field value of $B_{||} = 0.8$ T. In G_1 one can clearly see two peaks merging into a zero-bias conductance peak at the position of the QD resonance.